Advances in Computational Sciences and Technology
ISSN 0973-6107 Volume 7, Number 1 (2014) pp. 33-53

http://www.ripublication.com
https://dx.doi.org/10.37622/ACST/7.1.2014.33-53

# An Efficient Local Chan-Vese Expectation Maximization Model for Skull Stripping Magnetic Resonance Images of the Human Brain

**Gayatri Mirajkar and Dr. B. V. Barbadekar**

*PhD Scholar, Shivaji University, Kolhapur, India*
*Email: gayatrimirajkar@gmail.com*
*Research Guide, Shivaji University, Kolhapur, India*
*Email: balaji.barbadekar@gmail.com*

## Abstract

Skull stripping forms an important pre-processing step in neuroimaging analysis. In this paper, a local Chan-Vese Expectation Maximization (LCV-EM) model is proposed for skull segmentation which uses both global image information and the local information obtained via the Expectation Maximization (EM) algorithm. The energy functional for the proposed model consists of three terms: the global term, the local EM term, and the regularization term. Since magnetic resonance (MR) images contain a lot of intensity in homogeneity, the use of the local EM term along with the global term allows the segmentation of the brain from the skull and the non-brain tissue, in spite of the partial volume effect prominent near the boundary of the skull. The LCV-EM model is applicable to both T1 and T2-weighted MR images. The proposed model has the advantage that it does not require any boundary function or stopping function to decide the true boundary of the skull. Also the model shows good performance in comparison with other methods for brain extraction such as BSE, skull stripping using GAC, and the Chan-Vese model even in the presence of noise.

**Keywords:** MRI, skull stripping, active contours, expectation maximization, level sets

## 1. Introduction

Intracranial brain segmentation commonly referred to as skull-stripping, aims to segment the brain tissue (cortex and cerebellum) from the skull and non-brain intracranial tissues in MR images of the human brain. Skull stripping forms an important pre-processing step in neuroimaging analyses and is widely used in tasks such as multimodality image fusion and intersubject image comparisons, examination of the progression of brain disorders such as Alzheimer’s disease, multiple sclerosis, and schizophrenia, monitoring the development of ageing of the brain, and creating probability atlases from a large group of subjects [1]. Brain images are most typically skull-stripped before other processing algorithms such as registration, tissue classification, or bias-field correction are applied. The segmentation of the skull is also important in approaches which study various neurological disorders by aligning and normalizing a volumetric image of the intracranial cavity with respect to size and shape.

A number of factors complicate the problem of segmenting the skull in MRI volumes. These include partial volume effects, variable topology of the skull between individuals, regions of the skull with very high curvature, and regions of the skull whose thickness is very small as compared to the voxel size [2].

Skull stripping methods can generally be classified into three types: intensity-based, morphology-based, and deformable-model based. Intensity-based methods rely upon modeling the intensity distribution used for threshold classification. In [3], a semiautomated classification method is proposed for brain tissue classification in brain MR images. This method uses intensity distribution functions to identify major brain tissues (e.g., CSF, GM, and WM). Each brain tissue was modeled using a modified log-normal distribution function. The limitation for intensity-based methods is that they are frequently sensitive to intensity bias caused by magnetic field inhomogeneities, sequence variations, scanner drift, or random noise.

Morphology-based methods frequently combine connectivity-based morphological operations and thresholding or edge-detection to extract image features and identify brain surfaces. Lee et al. [4], proposed a 2D skull stripping method applied to a midsaggital slice, which was later extended by Huh et al. [5] to all slices in a saggital series. First, thresholds were used to separate dark pixels (e.g., background, skull, and cavities, etc) from bright pixels (e.g., brain, skin, facial tissues, etc), then brain regions were identified using a connectivity-based algorithm. Shattuck et al. [6] developed a tool called the brain surface extractor (BSE) which used a combination of edge detectors and morphological operators to skull-strip the brain. A Marr-Hildreth edge detector was first used to identify anatomic boundaries, then morphological operators were used to separate the tissues into component regions. Next, the largest central connected component was extracted as the brain region. Finally, nonbrain structures still attached to the brain region were removed. A potential disadvantage of these methods is that they are often dependent upon many parameters, and the parameters are often empirically generated and sensitive to small changes in the data.

Skull-stripping methods based upon deformable models typically evolve and deform an active contour to fit the brain surface, which is identified using separate image characteristic. Abountanos et al. [7] evolved a 2D contour by maximizing its corresponding 1D optimization problem, which was obtained via geometrical transformation from a 2D contour using dynamic programming techniques. The 1D optimization problem was described by a cost function that consisted of six terms including intensity value, morphology, gradient, moving speed of the contour, and smoothness of the contour. Zeng et al. [8] proposed a system of two level set equations whose zero level curves represented their inner and outer boundaries of the gray matter of the cortex. Each level set equation was driven towards the inner or outer boundary by a force term determined by the intensity distribution of brain tissues (i.e., CSF, WM, and GM). The two level set equations were further related to each other by constraining the distance between the inner and outer boundaries (i.e., the thickness of gray matter). Suri [9] proposed an active contour algorithm that uses the level set methods to evolve the active contour. A fuzzy membership function was used to classify the images into four components: WM, GM, CSF, and background, then a gradient detector was used along with a deformable model to evolve an active contour to fit the surface between CSF and GM. Ballard et al. [10] registered brain data to an atlas and used the brain surface from the atlas as the initial contour. Then, an equation based on the level set method was used, in which the speed term was determined by the curvature of the evolving surface and by a sign function that signaled whether to include or exclude a pixel that the curve passed. Smith [11] proposed an automated deformable model for skull stripping, called the brain extraction tool (BET), in which a set of forces, including morphological and image-based forces, were applied in the tangential and normal directions of the evolving surface. In general, deformable models have the potential to produce more robust and accurate skull-stripping results than methods using edge detection and threshold classification. Hybrid schemes have also been proposed to combine multiple results of different algorithms to compensate for problems encountered with individual methods [2]. In Zhuang et al. [1], an automatic algorithm called the model-based level set (MLS) method to remove the skull and intracranial tissues surrounding the brain in MR images. The level set method was used to evolve an active curve defined by the zero level set of the implicit function $\varphi$. The velocity of the evolving curve was determined by the image data and the morphology of the brain surface. The image data function was derived from the intensity value and the contrast between brain and non-brain tissues; the morphology term was derived from the mean curvature of the evolving surface.

In this paper, a local Chan-Vese Expectation Maximization (LCV-EM) model is proposed for skull segmentation which uses both global image information and the local information obtained via the EM algorithm. The energy functional for the proposed model consists of three terms: the global term, local-EM term, and the regularization term. Since MR images contain a lot of intensity inhomogeneity, the use of the local-EM term along with the global information allows the skull and non-brain tissue to be segmented from the brain tissue in spite of the partial volume effect prominent near the boundary of the skull.

The rest of the paper is organized as follows. Section II explains the partial volume effect and the partial volume model. Section III presents a brief review of the previous work pertaining to deformable active contours. The proposed LCV-EM model is explained in section IV along with its level set formulation and numerical implementation. Results and Discussion are presented in Section V. This also includes a comparison with other brain extraction algorithms (BEAs).

## 2. Partial Volume Effect

A problem with virtually all medical imaging devices is the partial volume effect (PVE); if the support of an image voxel overlays the boundary between two or more tissues, then the measured intensity value for that voxel will consist of a mixture of partial contributions from all the involved tissue types [12]. Intuitively, because the partial volume effect is caused by the limited spatial resolution of MRI, it should only appear at the boundaries of different tissue types and have a maximum influence width of 1 or 2 voxels across the boundaries. In practice, however the PVE affects a much wider area. The reason lies in the blurring effect of the imaging process, which has a diffuse point spread function effectively mixing the intensity of each voxel with many of its neighbors. Together with the PVE at tissue boundaries, the blurring effect depending on its strength and imaging quality makes the mixing effect of intensities from different tissue types appear in a wider area of the image [13].

### 2.1 Partial Volume Model

The brightness of a pixel on the (two-dimensional) screen represents the MR signal intensity from the 3D volume of tissue in the patient, and what is actually seen in the MR image is the front face of the voxel [14]. The pixel represents the signal obtained from the voxel element and is classically represented as a linear combination of pure class values present in the voxel. The MR signal $S$ from a voxel containing $m$ different tissues is given by,

$$S = \sum_{l=1}^{m} \left(\frac{V_l}{V}\right) S_l \tag{1}$$

where $V_l$ is the volume of the $l$-th tissue within the voxel, V is the total volume of the voxel, and $S_l$ is the signal from the $l$-th tissue. The grey level $P_{jk}$ of the (*j*, *k*)-th pixel corresponding to the (*j*, *k*)-th voxel in an MR image is given by,

$$P_{jk} = E\left[P_{jk}\right] + w_{jk} = \sum_{l=1}^{m} \left(\frac{V_{ljk}}{V}\right) S_l + w_{jk} \tag{2}$$

where $V_{ljk}$ is the partial volume of the $l$-th tissue in the (*j*, *k*)-th voxel, and $w_{jk}$ represents statistical noise that is assumed to be additive zero mean white Gaussian noise field, uncorrelated between different scenes of the same MRI sequence with standard deviation $\sigma$. $E\left[P_{jk}\right]$ is deterministic but unknown, whereas the noise $w_{jk}$ is stochastic, so the pixel gray level $P_{jk}$ is the sum of a deterministic value (to be estimated) and noise. The notation $E\left[P_{jk}\right]$ is used to denote the original, deterministic value of the pixel gray level, which contains information pertaining to partial volume averaging effects. To extract partial volume information, an image is generated whose pixel gray levels, on average, are proportional to the percentages of a specific tissue in the corresponding voxels [15].

Pure bone class is not strongly present in the neighborhood of thin bone. Fig. 1(a) shows the real-world situation in which each point is exactly one type of material. Fig. 1(b) shows the sampling process which creates a band of mixture of the two materials between materials A and B. Points $P_1$ and $P_2$ lie in the two materials A and B respectively. However, point $P_3$ lies in the transition band/region between the two materials where they are mixed. The transition band contains the partial volume pixels which contains the signal mixture from both the tissue types A and B. If we consider zone A as bone (BN) and zone B as tissue (TS) then the mixture zone contains pixels whose signal intensity is a mixture of bone (BN) and tissue (TS) depending on their proportions present in the corresponding voxel. By tissue it is meant to consider all types of tissue other than bone.

Let the gray level values of tissue and bone be $M_{tissue}$ and $M_{bone}$ respectively. For the transition region between the pure zones A and B, the gray level value of a pixel can be given by,

$$g = \alpha_{bone} \cdot M_{bone} + \alpha_{tissue} \cdot M_{tissue}$$

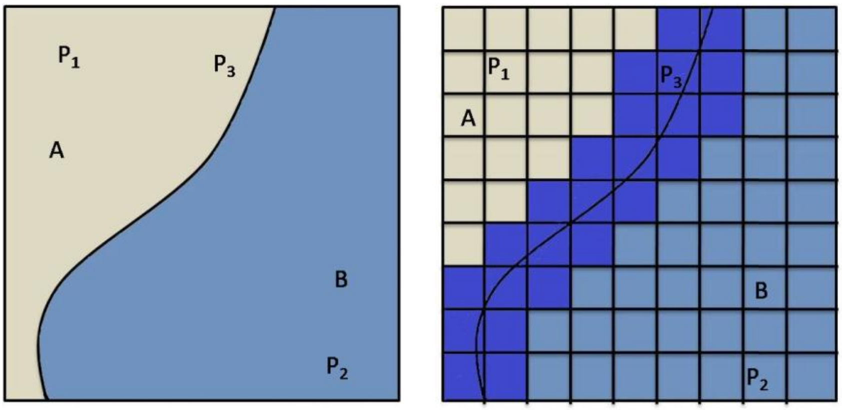

(a) (b)

**Figure 1. Zone with bone (A) and tissue regions (B) (a) real world situation, (b) discrete image created by the sampling process**

where $\alpha_{bone}$ is the corresponding percentage of bone present and $\alpha_{tissue}$ is proportional to the percentage of tissue present. $M_{bone}$ and $M_{tissue}$ are unknown and can be estimated. Actually, the problem can be viewed as a classification problem in which the transition region pixels need to be classified according to their gray-level values which in turn are dependent on the percentage of bone and tissue present in the corresponding voxel.

As mentioned earlier PVE is a problem associated with all medical imaging devices. In fact, several tissue types surround the skull. The global tissue characterization in the image as proposed by Santago and Gage [16] is not suited to the problem. In Desco et al. [17], an automatic segmentation procedure for MRI neuroimages that overcomes part of the problems involved in multidimensional clustering techniques like partial volume effects (PVE), processing speed and difficulty of incorporating a priori knowledge. The method is a three-stage process in which expectation-maximization algorithms are used to estimate the probability density function (pdf) of the pixels, which are assumed to be mixtures of Gaussians. Balafar [18] proposed an improvement of the EM algorithm for MRI brain image segmentation. In order to improve EM performance, the proposed algorithm incorporates neighborhood information into the clustering process. In Pham and Prince [19], a general framework for performing robust, unsupervised tissue classification is presented. Tissue classification is formulated as an estimation problem based on an imaging model. Prior models are used within the estimation problem to compensate for noise and intensity. In Leemput et al. [20], a statistical framework for partial volume segmentation that encompasses and extends existing techniques is proposed. They started from a commonly used parametric statistical image model in which each voxel belongs to one single tissue type, and introduce an additional downsampling step that causes partial voluming along the borders between tissues. An expectation-maximization approach is used to simultaneously estimate the parameters of the resulting model and perform a PV classification.

As described earlier PVEs occur where multiple tissues contribute to a single voxel, resulting in blurring of edges at the boundary. Because of PVEs, it is often desirable to allow for some uncertainty in tissue classification. So-called soft segmentations allow multiple tissues to exist at a particular location with different levels of membership or probability. Unlike the kmeans algorithm, the approaches based on Gaussian clustering via the expectation-maximization (EM) algorithm are capable of producing soft segmentation that can better model PVEs by computing a posterior probability at each pixel [21-23].

In the proposed method, two classes are assumed, namely bone and tissue. By tissue it is meant that all tissues other than bone are considered. Estimation of the unknown pixel class as well as class probabilities and class means is done using EM algorithm. The class probabilities signify the percentage of bone and tissue in the region surrounding the evolving contour. By incorporating these class means in the deformable model, the contour can be made to evolve such that it contains the brain tissue effectively bypassing the partial volume pixels classified as belonging to the bone class by the EM algorithm. The contour evolution is stopped after a specific number of iterations are completed or when the contour reaches stability.

## 3. Previous Works

### 3.1 Mumford-Shah Model

The Chan-Vese model is the curve evolution implementation of a piecewise constant case of the Mumford-Shah model [24]. Mumford-Shah model is an energy-based method introduced by Mumford and Shah via an energy functional. The basic idea is to find a pair of ($u$, $C$) for a given image $u_0$, where $u$ is a nearly piecewise approximation of $u_0$ and C denotes the smooth and closed segmenting curve.

The general form for the Mumford-Shah energy functional can be written as follows,

$$E^{MS}(u,C) = \int_{\Omega} |u_0(x,y) - u(x,y)|^2 dxdy + \mu \int_{\Omega \backslash C} |\nabla u(x,y)|^2 dxdy + \nu \cdot Length(C) \quad (3)$$

where $\mu$ and $\nu$ are positive constants, $\Omega$ denotes the image domain, the segmenting curve $C \subset \Omega$. To solve the Mumford-Shah problem is to minimize the energy functional over $u$ and $C$. The removal of any of the above 3 terms in exp. (3) will result in trivial solutions for u and C [24]. However, with all 3 terms, it becomes a difficult problem to solve since $u$ is a function in the $N$-dimensional space ($N$=2 in 2D image segmentation), while $C$ is an ($N$-1) dimensional data set.

### 3.2 Chan-Vese Model:

The Chan-Vese (CV) model [25] is an alternative solution to the Mumford-Shah problem which solves the minimization of exp. (3) by minimizing the following energy functional:

$$\begin{aligned} E^{CV}(c_1, c_2, C) &= \mu \cdot Length(C) \\ &+ \lambda_1 \int_{inside(C)} |u_0(x,y) - c_1|^2 dxdy \\ &+ \lambda_2 \int_{outside(C)} |u_0(x,y) - c_2|^2 dxdy \end{aligned} \tag{4}$$

where $\mu$, $\lambda_1$, and $\lambda_2$ are positive constants, usually fixing $\lambda_1 = \lambda_2 = 1$, $c_1$ and $c_2$ are the intensity averages of $u_0$ inside $C$ and outside $C$ respectively.

To solve this minimization problem, the level set method [26] is used which replaces the unknown curve $C$ by the level-set function $\phi(x,y)$, considering that $\phi(x,y) > 0$ if the point (x, y) is inside $C$, $\phi(x,y) < 0$ if (x, y) is outside $C$, and $\phi(x,y) = 0$ if (x, y) is on $C$. Thus, the energy functional $E^{CV}(c_1, c_2, C)$ can be reformulated in terms of the level set function $\phi(x,y)$ as follows:

$$\begin{aligned} E_\varepsilon^{CV}(c_1, c_2, \phi) &= \mu \int_\Omega \delta_\varepsilon\big(\phi(x,y)\big)|\nabla\phi(x,y)|dxdy \\ &+ \lambda_1 \int_\Omega |u_0(x,y) - c_1|^2 H_\varepsilon\big(\phi(x,y)\big)dxdy \\ &+ \lambda_2 \int_\Omega |u_0(x,y) - c_2|^2 (1 - H_\varepsilon\big(\phi(x,y)\big))dxdy \end{aligned} \tag{5}$$

where $H_\varepsilon(z)$ and $\delta_\varepsilon(z)$ are respectively, the regularized approximations of the Heaviside function $H(z)$ and the Dirac Delta function $\delta(z)$ as follows:

$$H(z) = \begin{cases} 1, if\ z \geq 0 \\ 0, if\ z < 0 \end{cases}$$

$$\delta_0(z) = \frac{d}{dz} H(z) \tag{6}$$

The minimization problem is solved by taking the Euler-Lagrange equations and updating the level set function $\phi(x,y)$ by the gradient descent method:

$$\frac{\partial\phi}{\partial x} = \delta_\varepsilon(\phi)\left[\mu\, div\left(\frac{\nabla\phi}{|\nabla\phi|}\right) - \lambda_1|u_0 - c_1|^2 + \lambda_2|u_0 - c_2|^2\right] \tag{7}$$

where $c_1$ and $c_2$ can be respectively updated at each iteration by

$$c_1(\phi) = \frac{\int_\Omega u_0(x,y)H\big(\phi(x,y)\big)dxdy}{\int_\Omega H\big(\phi(x,y)\big)dxdy}$$

$$c_2(\phi) = \frac{\int_\Omega u_0(x,y)(1 - H\big(\phi(x,y)\big))dxdy}{\int_\Omega (1 - H\big(\phi(x,y)\big))dxdy} \tag{8}$$

The Chan-Vese model has achieved good performance in image segmentation task due to its ability of obtaining a larger convergence range and handling topological changes naturally. It can deal with the detection of objects whose boundaries are either smooth or not necessarily defined by gradient. In such cases, the edge-based level set methods commonly fail and result in boundary leakage [27]. Second, it does not require image smoothing and thus can efficiently process the images with noise. Therefore, the true boundaries are preserved, and could be accurately detected. However, the CV model suffers from some intrinsic limitations. The CV model generally works for images with intensity homogeneity since it assumes that the intensities in each region remains constant. The CV model thus leads to poor segmentation results for images with intensity inhomogeneity due to wrong movement of evolving curves guided by global image information. Second, the segmentation of CV model is usually dependent on the placement of the initial contour, especially for the complicated images. Sometimes, different results will be obtained for the same image by using different initial contours.

## 4. Local Chan-Vese Expectation Maximization Model

The proposed local Chan-Vese EM (LCV-EM) model is discussed along with its numerical implementation. The proposed model is defined based on the techniques of curve evolution, local statistical function, and level set methods. MR images contain a lot of intensity inhomogeneity in them, i.e., the intensity changes over the image due to the varied amount of tissues in them. Therefore, traditional level set methods, using either the image gradient [30-32] or the global information [25], [33] to drive the evolving curve(s) towards the true boundaries cannot achieve success in segmentation of the skull from surrounding tissue. The proposed model combines both local and global statistical information to overcome the inhomogeneous distribution in the MR image and hence provide more satisfactory segmentation of the skull from the surrounding tissue.

The overall energy functional in the proposed LCV-EM model consists of three parts: the global term $E^G$, the local EM term $E^{L\text{-}EM}$ and the regularization term $E^R$. Thus, the overall energy functional can be described as,

$$E^{LCV-EM} = \alpha \cdot E^G + \beta \cdot E^{L-EM} + E^R \tag{9}$$

### 4.1 Global Term

The global term $E^G$ is derived directly from exp. (4) in the Chan-Vese model, in which it is called as the fitting term. It can be seen that the global term is defined based on the global properties, i.e., the averages of $u_0$ inside $C$ and outside $C$, which is stated as follows:

$$\begin{aligned} E^G(c_1, c_2, C) &= F_1(C) + F_2(C) \\ &= \int_{inside(C)} |u_0(x,y) - c_1|^2 dxdy + \int_{outside(C)} |u_0(x,y) - c_2|^2 dxdy \end{aligned} \tag{10}$$

Using the level set formulation, the boundary $C$ is represented using the zero level set of a Lipschitz function $\phi\colon \Omega \to R$.

$$\phi(x,y) = \begin{cases} > 0 \; if \; (x,y) is \; inside \; C \\ = 0 \; if \; (x,y) is \; on \; C \\ < 0 \; if \; (x,y) is \; outside \; C \end{cases} \tag{11}$$

Accordingly, the global term in exp. (10) can be rewritten so as to evaluate the level set function $\phi$ on the domain $\Omega$:

$$E^G(c_1, c_2, C) = \int_\Omega |u_0(x,y) - c_1|^2 H\big(\phi(x,y)\big)dxdy + \int_\Omega |u_0(x,y) - c_2|^2 (1 - H(\phi(x,y)))dxdy \tag{12}$$

where, $H(z)$ is the Heaviside function described in exp. (6). Usually, after exp. (12) comes to a steady state, or approximately to be zero, the evolving curve $C$ (the zero level set of $\phi$) will separate the object from the background. However, for the images with intensity inhomogeneity such as MR images, the final obtained curve can hardly divide the image into object region and background region even after a long iteration time. The reason is that the global term assumes that the image intensity is piecewise constant like the CV model. Thus, the averages $c_1$ and $c_2$ act as the global information and cannot represent the inhomogeneous intensities of the object region and background region in the images with intensity inhomogeneity. Therefore, to achieve a good performance in segmenting the images with intensity inhomogeneity, the local image information needs to be included [44].

### 4.2 Local Chan-Vese Expectation-Maximization Term

The following local term is introduced which uses the local statistical information as the key improvement factor for improving the segmentation performance on MR images, showing large intensity inhomogeneity.

$$E^{L-EM}(\mu_1, \mu_2, C) = \int_{inside(C)} |u_0(x,y) - \mu_1|^{\alpha_1} dxdy + \int_{outside(C)} |u_0(x,y) - \mu_2|^{\alpha_2} dxdy \tag{17}$$

where $\mu_1$ and $\mu_2$ are the class means obtained by the application of the EM algorithm to narrowbands surrounding the evolving contour both on the inside and outside respectively considering the two classes, i.e., bone and tissue. A description of the EM algorithm can be found in [43]. The level set formulation allows for the narrowband implementation of the model, and also allows for the application of the EM algorithm to narrowbands on the inside and outside of the evolving contour, which is an important factor as this results in an considerable decrease of the computation time. Too small a width of the surrounding narrowbands will not be adequate to cover the partial volume pixels between the boundary of the skull and the brain tissue. Too large a width will also not be adequate as this will make the overall speed of computation too slow. It was found experimentally that a width of 5-20 pixels is adequate. The local fitting term keeps on decreasing while the curve evolves towards the true boundaries of objects in the image, and the true boundary $C^*$ is a minimizer of the following fitting term:

$$\inf_{C}(F_1^{L-EM}(C) + F_2^{L-EM}(C)) \approx 0 \approx F_1^{L-EM}(C^*) + F_2^{L-EM}(C^*) \tag{18}$$

where $F_1^{L-EM}(C) + F_2^{L-EM}(C)$ denotes the local fitting term. In a manner similar to the global term, the local term exp. (17) can also be reformulated in terms of the level set function $\phi(x, y)$ as follows:

$$\begin{aligned} E^{L-EM}(\mu_1, \mu_2, C) &= \int_{\Omega} |u_0(x, y) - \mu_1|^{\alpha_1} H\big(\phi(x, y)\big) dxdy \\ &+ \int_{\Omega} |u_0(x, y) - \mu_2|^{\alpha_2} \Big(1 - H\big(\phi(x, y)\big)\Big) dxdy \end{aligned} \tag{19}$$

### 4.3 Regularization Term

To control the smoothness of the zero level set and further avoid the occurrence of small, isolated regions in the final segmentation, a length penalty term $L(C)$ is added as the regularization term.

Let $C$ be a smooth closed planar curve $C(p): [0, 1] \rightarrow \Omega$ parameterized by parameter $p \in [0, 1]$. The length functional can be written as,

$$L(C) = \oint_C dp \tag{20}$$

Replacing the curve C by the level set function, $\phi(x, y)$, $L(C)$ can be reformulated as,

$$L(\phi = 0) = \int_{\Omega} |\nabla H(\phi(x, y))| dxdy = \int_{\Omega} \delta(\phi(x, y)) |\nabla \phi(x, y)| dxdy \tag{21}$$

where, $H(z)$ is the Heaviside function and $\delta(z)$ the Dirac Delta function, which has been described in exp. (6). The use of length penalty term implies that the evolving curve which minimizes the overall energy functional should be as short as possible. It imposes a penalty on the length of the curve that separates the two phases of the image, i.e., foreground and background on which the energy functional will make a transition from one of its values $c_1(\mu_1)$ to $c_2(\mu_2)$.

In many situations, the level set function will develop shocks, very sharp and/or flat shape during the evolution, which in turn makes further computation highly inaccurate in numerical approximations. To avoid these problems, it is necessary to reshape the level set function to a more useful form, while keeping the zero location unchanged. A common numerical scheme is to reinitialize the function $\phi(x, y)$ to be a signed distance function periodically during the evolution, which can be written as,

$$\phi(x, y) = \begin{cases} dist(X, C_t) \; if \; X \; is \; inside \; C_t \\ 0 \; if \; X \in C_t \\ -dist(X, C_t) \; if \; X \; is \; outside \; C_t \end{cases} \tag{22}$$

where, $dist(X, C_t)$ is the shortest Euclidean distance of $X$ to the points on the evolving curve $C_t$ at time t. It is crucial to keep the evolving level set function as an approximate signed distance function during the evolution, especially in the neighborhood around the zero level set [38]. The most straightforward way of implementing the reinitialization operation is to extract the zero level set and then compute the distance function from it.

However, the method is generally time-consuming. To, overcome this difficulty, a now widely accepted method has been proposed in [39] in order to re-initialize the level set function by solving the following partial-difference expression:

$$\frac{\partial \phi}{\partial t} = sign(\phi_0)(1 - |\nabla \phi|) \tag{23}$$

where $\phi_0$ is the function to be re-initialized, and $sign(\phi_0)$ is the sign function. When the steady state of exp. (23) is reached, $\phi$ will be a distance function with the same zero level set as $\phi_0$ despite $\phi_0$ is a distance function or not. This is commonly known as the standard re-initialization procedure.

### 4.3 Level Set Formulation

In the level set formulation, the curve $C$ is represented by the zero level set of a Lipschitz function $\phi$. The overall energy functional in exp. (9) can be further described as follows:

$$E^{LCV-EM}(c_1, c_2, \mu_1, \mu_2, \phi) = \alpha \cdot E^G(c_1, c_2, \phi) + \beta \cdot E^{L-EM}(\mu_1, \mu_2, \phi) + E^R(\phi \tag{24}$$

where, $\alpha$ is a positive parameter, and $\beta$ can be positive or negative, which govern the trade-off between the global term and the local-EM. In the experiments carried out $\alpha = 1$ and $\beta = -1$.

In general, the skull segmentation process can be equivalently transformed into finding a solution that minimizes $E^{LCV-EM}$ by evolving the level set function $\phi$. The Heaviside function $H(z)$ and the Dirac Delta function $\delta(z)$ described in exp. (6) are then applied to divide the level set function into three parts, i.e., the part inside $C$, the part outside $C$, and the part on $C$. For practical and feasible implementation, $H_\varepsilon(z)$ is chosen as a non-compactly supported, smooth and strictly monotone approximation of $H(z)$, which can be written as,

$$H_\varepsilon(z) = \frac{1}{2}\left|1 + \frac{2}{\pi} arctan \left|\frac{z}{\varepsilon}\right|\right|, \varepsilon \to 0 \tag{25}$$

The regularized approximation $\delta_\varepsilon(z)$ of Dirac Delta function $\delta(z)$ is correspondingly computed by

$$\delta_\varepsilon(z) = \frac{1}{\pi}\frac{\varepsilon}{\varepsilon^2 + z^2} \tag{26}$$

Therefore, the overall energy functional can then be rewritten as,

$$\begin{aligned} E^{LCV-EM}&(c_1, c_2, \mu_1, \mu_2, \phi) \\ &= \int_\Omega (\alpha \cdot |u_0(x,y) - c_1|^2 + \beta \cdot |u_0(x,y) - \mu_1|^{\alpha_1}) \times H_\varepsilon(\phi(x,y))dxdy \\ &+ \int_\Omega (\alpha \cdot |u_0(x,y) - c_2|^2 + \beta \cdot |u_0(x,y) - \mu_2|^{\alpha_2}) \\ &\times (1 - H_\varepsilon(\phi(x,y)))dxdy + \mu \cdot \int_\Omega \delta_\varepsilon(\phi(x,y))|\nabla \phi(x,y)|dxdy \end{aligned} \tag{27}$$

The gradient descent method is used to compute the minimizer of exp. (27). For a fixed level set function $\phi$, we minimize the energy functional in exp. (27) with respect to the two pairs of constants $c_1$ and $c_2$, $\mu_1$ and $\mu_2$. By calculus of variations it can be shown that the constant functions $c_1(\phi)$ and $c_2(\phi)$ that minimize $E^{LCV-EM}(c_1, c_2, \mu_1, \mu_2, \phi)$ for a fixed function $\phi$ are given by,

$$c_1(\phi) = \frac{\int_\Omega u_0(x,y) H_\varepsilon(\phi(x,y))dxdy}{\int_\Omega H_\varepsilon(\phi(x,y))dxdy} \qquad (28a)$$

$$c_2(\phi) = \frac{\int_\Omega u_0(x,y)(1-H_\varepsilon(\phi(x,y)))dxdy}{\int_\Omega (1-H_\varepsilon(\phi(x,y)))dxdy} \qquad (28b)$$

It is obtained experimentally that,

$$\mu_1(\phi) = \min(\mu_{11}, \mu_{12}) \qquad (29a)$$

$$\mu_2(\phi) = \min(\mu_{21}, \mu_{22}) \qquad (29b)$$

where, $\mu_{11}$, $\mu_{12}$, and $\mu_{21}$, $\mu_{22}$ are the class means obtained from the EM algorithm for the assumed two classes bone and tissue, derived from the interior and exterior narrowbands respectively surrounding the evolving contour. Accordingly, $c_1$, $c_2$, $\mu_1$, $\mu_2$ are also changing with respect to the evolving contour *C*.

The minimization of exp. (27) can be done by introducing an artificial time variable $t \geq 0$, and moving $\phi$ in steepest descent direction to a steady state with the initial condition defined in exp. (30b), and boundary condition defined in exp. (30c):

$$\frac{\partial \phi}{\partial t} = \delta_\varepsilon(\phi)\left[-\left(\alpha(u_0 - c_1)\right)^2 + \beta(u_0 - \mu_1)^{\alpha_1}) + (\alpha(u_0 - c_2)^2 + \beta(u_0 - \mu_2)^{\alpha_2}\right] + \mu\delta_\varepsilon(\phi) div\left(\frac{\nabla\phi}{|\nabla\phi|}\right) (30a)$$

$$\phi(0, x, y) = \phi_0(x, y)\ in\ \Omega \qquad (30b)$$

$$\frac{\partial \phi}{\partial \bar{n}} = 0 \text{ on } \partial\Omega \qquad (30c)$$

where $\bar{n}$ denotes the exterior normal to the boundary $\partial\Omega$. In the above partial differential expression, the Neumann boundary condition in exp. (30c) is chosen as the boundary condition. Usually, Neumann boundary condition has many advantages. First, it is easy to implement since there are no values to assign for $\phi$ at the boundary. Second, it implies that the solution of exp. (27) satisfies a maximum principle. Moreover the gaps of the curve *C* may appear only when advancing the zero level set which would change its topology, and cannot come from outside of $\Omega$ because of the spurious values created by the Neumann boundary condition.

### 4.4 Termination Criteria for Curve Evolution

The evolving curve *C*, or the zero level set function, will gradually split according to the topological structure of the object and evolves towards the true boundaries of objects in images. When evolving curves finally arrive at the position of the true boundary $C^*$, the curves should stop evolving. Now, a problem of when and how the curves automatically stop evolving or what termination criterion is for curves evolution is arising.

It can be obviously seen that the global term and the local-EM term keeps decreasing while the curve evolves towards the true boundaries of objects, and the true boundary $C^*$ is the minimizer of the global term and the local term, which can be written as follows:

$$\inf_C(\alpha \cdot E^G(C) + \beta \cdot E^{L-EM}(C)) \approx 0 \approx \alpha \cdot E^G(C^*) + \beta \cdot E^{L-EM}(C^*) \qquad (31)$$

In the implementation, the termination criterion chosen is the steady-state reached by the contour. When the curve reaches the true boundary, it will remain stable. Hence, the curve evolution process is stopped, when either the fixed number of iterations are completed or when the evolving contour reaches its steady state.

### 4.5 Numerical Implementation of the Model:

The partial differential expression in the continuous domain defined in exp. (30a) can be solved by a finite difference method in the numerical scheme. All the spatial partial derivatives are approximated by the forward difference. Then exp. (30a) can be discritized using the forward difference as follows:

$$\frac{\phi_{i,j}^{n+1}-\phi_{i,j}^{n}}{\Delta t} = L\left(\phi_{i,j}^{n}\right) \tag{32}$$

Where $\Delta t$ is the time step and $L\left(\phi_{i,j}^{n}\right)$ is the numerical approximation of the right hand side in exp. (30a). The corresponding curvature $\kappa = div\left(\frac{\nabla\Phi}{|\nabla\phi|}\right)$ in the $L\left(\phi_{i,j}^{n}\right)$ can be discretized using a second-order central difference scheme:

$$\kappa = div\left(\frac{\nabla\Phi}{|\nabla\phi|}\right) = \frac{\phi_{xx}\phi_y^2-2\phi_{xy}\phi_x\phi_y+\phi_{yy}\phi_x^2}{\left(\phi_x^2+\phi_y^2\right)^{3/2}} \tag{33}$$

where $\phi_x, \phi_y, \phi_{xx}, \phi_{yy}$ are computed as follows:

$$\begin{aligned}
\phi_x &= \frac{1}{2h}\left(\phi_{i+1,j}-\phi_{i-1,j}\right)\\
\phi_y &= \frac{1}{2h}\left(\phi_{i,j+1}-\phi_{i,j-1}\right)\\
\phi_{xx} &= \frac{1}{h^2}\left(\phi_{i+1,j}+\phi_{i-1,j}-2\phi_{i,j}\right)\\
\phi_{yy} &= \frac{1}{h^2}\left(\phi_{i,j+1}+\phi_{i,j-1}-2\phi_{i,j}\right)\\
\phi_{xy} &= \frac{1}{h^2}\left(\phi_{i+1,j+1}-\phi_{i-1,j+1}-\phi_{i+1,j-1}+\phi_{i-1,j-1}\right)
\end{aligned} \tag{34}$$

where $h$ is the grid spacing. Exp. (30a) can then be implemented as follows:

$$\begin{aligned}
\frac{\phi_{i,j}^{n+1}-\phi_{i,j}^{n}}{\Delta t} &= \delta_\varepsilon\left(\phi_{ij}^{n}\right)\left\{-\left(\alpha\left(u_{ij}-c_1(\phi^n)\right)^2+\beta\left(u_{ij}-\mu_1(\phi^n)\right)^{\alpha_1}\right)\right.\\
&\quad \left.+\left(\alpha\left(u_{ij}-c_2(\phi^n)\right)^2+\beta\left(u_{ij}-\mu_2(\phi^n)\right)^{\alpha_2}\right)\right\}+\mu\cdot\delta_\varepsilon\left(\phi_{ij}^{n}\right)\kappa
\end{aligned} \tag{35}$$

where $\delta_\varepsilon$ and $\kappa$ are computed according to exp.(25) and exp. (33) respectively.

### 4.6 Description of Algorithm Steps

A description of the algorithm of LCV-EM is given as follows. It consists of the following steps:

Step 1: Input the original image $u_0$.

Step 2: Set the initial curve $C_I$ in $u_0$. Set the value of time step $\Delta t$, the grid spacing $h$ and $\varepsilon$ in exp. (34). In practice $\Delta t = 0.1$ and $h = \varepsilon = 1$. Set the values of the controlling parameter of the global term i.e., $\alpha$, the controlling parameter of the local term i.e., $\beta$, and the length controlling parameter $\mu$. For MR images, $\alpha = 1$, $\beta = -1$, and $\mu = 1$.

Step 3: Evolve level set function $\phi$ according to exp. (30) and its numerical solution scheme described in exp. (35).

Step 4: Extract the evolving curve $C$ from the zero level set function.

Step 5: Decide whether the termination criterion described in section 4.4 is satisfied or not.

Step 6: If yes, the algorithm is stopped, otherwise go to step 3.

## 5. Results and Discussion

The brain extraction algorithms using the LCV-EM model has been developed using MATLAB 2009b on an Intel Pentium Core2Duo machine. The images used for the analysis have been taken from the Open Access Series of Imaging Studies (OASIS) and The Whole Brain Atlas. Out of the two datasets available on the OASIS webpage, the dataset of cross-sectional MRI data in young, middle-aged, nondemented, and demented older adults is used. Both T1-and T2-weighted MR images are used for the analysis. During the implementation of the LCV-EM model, no pre-processing steps such as morphological filtering or anisotropic diffusion was employed. The initial contour was interactively placed to be near the brain-skull interface using the roipoly function in MATLAB. This has the advantage of reducing the number of iterations and also bypasses the structures present within the brain (e.g., tumors etc.). Also a reduction in the number of iterations is achieved. In the implementation, the time step *dt* is calculated using the Courant-Fredrichs-Lewy condition.

The segmentation results for the images from the OASIS dataset are shown in fig. 2. Fig. 2(a) is showing the original brain MR image from the OASIS dataset. The slice orientation chosen for analysis is the transaxial or axial orientation. The processed skull stripped result for the corresponding image present in the dataset is shown in fig. 2(d). This is taken as the gold standard for comparison with other methods including the proposed method. Fig. 2(b) and fig. 2(c) are showing the MR image with the developed contour superimposed on it. Fig. 2(e) is showing the result of the proposed method with the values of $\alpha_1 = \alpha_2 = 5$ and fig. 2(f) is showing the result of the proposed model with the values of $\alpha_1 = \alpha_2 = 11$. On observing both images, i.e., fig. 2(e) and fig. 2(f) it can be seen that the parameters $\alpha_1$ and $\alpha_2$ indeed control the ability of the model to follow the curves in the original image. A small value of $\alpha_1$ and $\alpha_2$ allows the model to follow the curves of the brain more closely, while large values of $\alpha_1$ and $\alpha_2$ make the proposed model to obtain coarse segmentation.

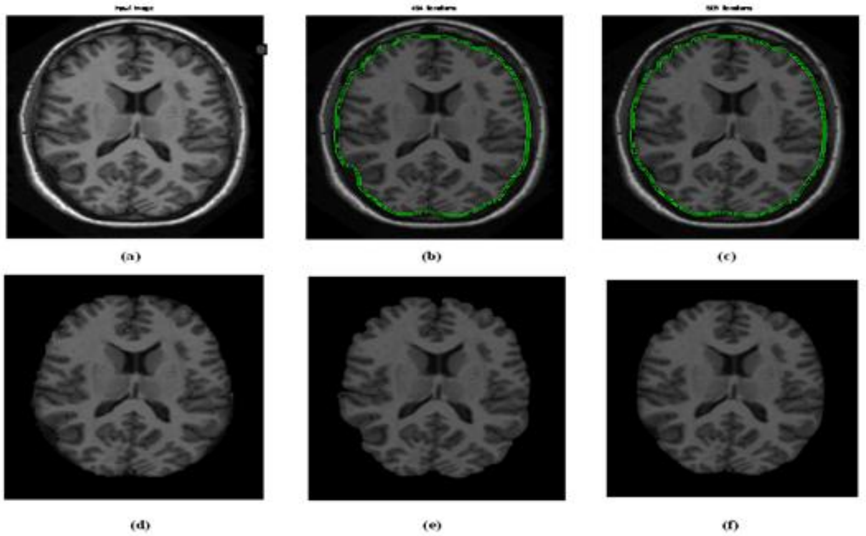

**Figure 2. Skull stripping results for the proposed model (a) Original image (b)**

**MR image with contour overlayed on it ($\alpha_1 = \alpha_2 = 5$), (c) MR image with contour overlayed on it ($\alpha_1 = \alpha_2 = 11$) (d) Processed image with skull stripped from the OASIS dataset (e) Result obtained from the LCV-EM model for $\alpha_1 = \alpha_2 = 5$, (f) Result obtained from the LCV-EM model for $\alpha_1 = \alpha_2 = 11$**

Fig. 3 is showing the results of the proposed algorithm applied to T1-, T2-, and T2*-weighted images. Fig. 3(a) is showing the T1-weighted image, fig. 3(b) is showing the T2-weighted image and fig. 3(c) is the T2*-weighed image. Fig. 3(d), fig. 3(e), and fig. 3(f) are the corresponding skull segmented results for T1-, T2-and T2*-weighted images respectively. It is observed that as compared to other active contour models, segmentation using LCV-EM is more reliable and also depends upon a lesser number of parameters. The calculation time is further reduced by using narrow-band propagation of the model. The proposed model is also insensitive to random noise scattered in the MR image.

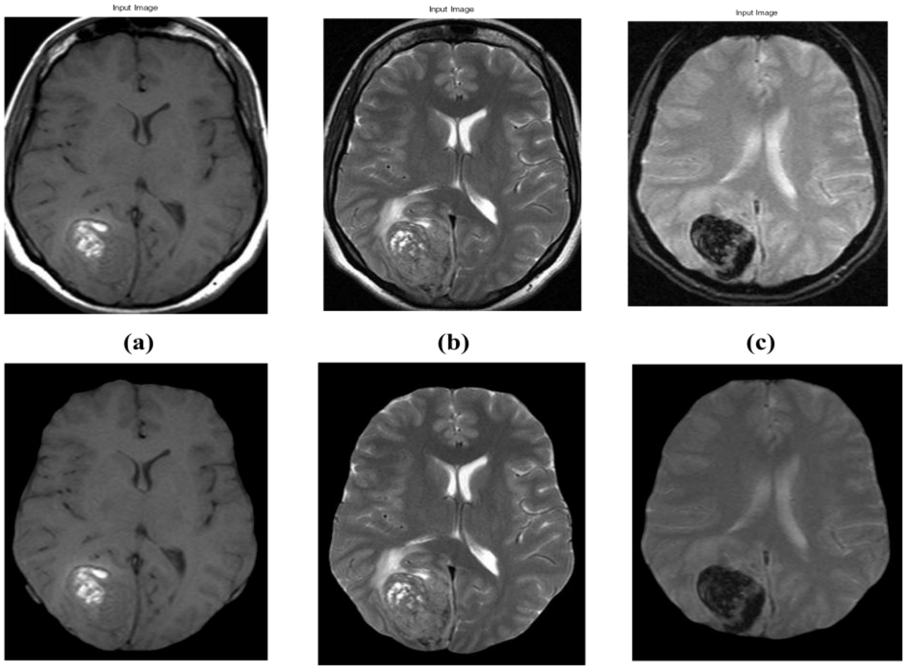

(a) (b) (c)

(d) (e) (f)

**Figure 3. Skull stripping results using LCV-EM for (a), (d) axial T1 weighted, (b), (e) axial T2 weighted, (c), (f) axial T2* weighted**

To evaluate the performance of the proposed model, its results are compared with well-known skull stripping methods such as the Brain Surface Extractor (BSE) algorithm, skull stripping using geodesic active contours (GAC) [40], and the Chan-Vese model [25]. The processed results available in the OASIS dataset are taken as the gold standard. The BSE algorithm is available in the stand alone application Brain Suite which is available for download via http: /users.loni.ucla.edu. Fig. 4 is showing the skull segmentation results for BSE, GAC, Chan-Vese active contour model, and the proposed LCV-EM model. The disadvantage of the GAC algorithm is its dependence on the stopping function. The accuracy of the algorithm depends on the stopping function generated. The more accurate the stopping function is able to highlight the boundary between the brain and non-brain region, the more accurate, the GAC is able to follow the curves in the brain region. The presence of a weak boundary or a kink in the detected boundary can cause leakage of the contour through that portion, resulting in incorrect segmentation. As opposed to this, the LCV-EM model does not require any stopping function. Also, the problem of leakage through the boundary can also be eliminated through the choice of the width of the interior and exterior bands surrounding the narrowband representing the evolving contour. Evaluation of the performance of the proposed LCV-EM model is first done using FPR as the evaluation parameter. Table 1 is showing the FPR for all four BEAs, namely BSE, skull stripping using GAC, Chan-Vese active contour model, and the LCV-EM model. It can be seen that LCV-EM model provides the optimum performance with respect to that of the other algorithms. It is also observed that the FPR for the GAC algorithm is slightly larger than that of BSE and LCV-EM. This can be attributed mainly to the conservative nature of the algorithm, i.e., the tendency to avoid removing non-brain tissus [40]. The performance of the Chan-Vese model is somewhat poor as compared to that of BSE and LCV-EM. This is because the model tends to align itself along the deep sulci of the brain. The addition of the L-EM term reduces this tendency and improves the performance of the model.

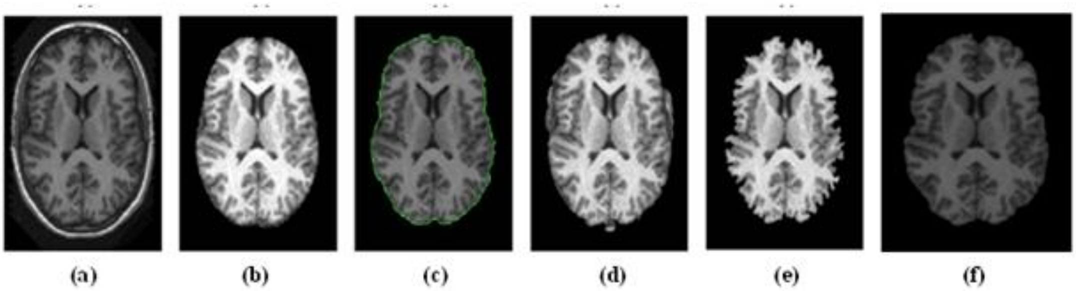

**Figure 4. Skull stripping results (a) Original image (b) processed standard (c) BSE (d) GAC (e) Chan-Vese active contour model (f) LCV-EM model**

**Table 1. Performance indices of GAC, Chan-Vese active contour model, BSE, and LCV-EM models of skull stripping**

| Sr. No. | Method | FP_rate |
|---|---|---|
| 1 | GAC | 0.0489 |
| 2 | Chan-Vese Active Contours | 0.1369 |
| 3 | BSE | 0.0265 |
| 4 | LCV-EM | 0.0193 |

Fig. 6 is showing the segmentation results for LCV-EM model, BSE, and the Chan-Vese models. The first column of fig. 6 is showing the original images taken from the OASIS dataset. The second column shows the processed results present in the dataset against which comparison of the BEAs is made. The third column contains the results of LCV-EM model for the respective images. The fourth column contains skull segmentation results for BSE and the last column contains skull segmentation results obtained using the Chan-Vese Model. The corresponding performance indices, i.e., the Jaccard coefficient, Dice coefficient, false positive rate and false negative rate are shown in Table 2. It can be observed from fig. 5 as well as table 2, that LCV-EM provides better results than both BSE and Chan-Vese algorithms.

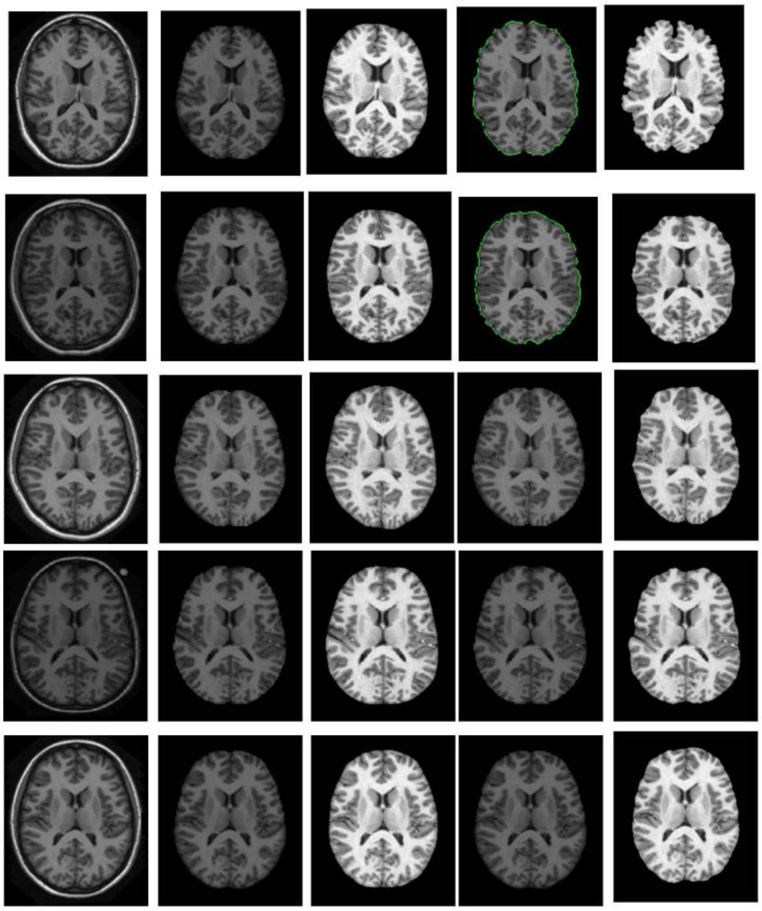

**Figure 5. Skull stripping results for LCV-EM, BSE, and Chan-Vese model**

**Table 2. Performance Indices for LCV-EM, Chan-Vese, and BSE skull stripping methods**

| Sr. No. | Image | LCV-EM Model | | | | Chan-Vese | | | | BSE | | | |
|---|---|---|---|---|---|---|---|---|---|---|---|---|---|
| | | J | D | FPR | FNR | J | D | FPR | FNR | J | D | FPR | FNR |
| 1 | Img1 | 0.9621 | 0.9807 | 0.0065 | 0.0316 | 0.9005 | 0.9477 | 0.0005 | 0.0990 | 0.9422 | 0.9702 | 0.0406 | 0.0195 |
| 2 | Img2 | 0.9374 | 0.9677 | 0.0016 | 0.0611 | 0.8613 | 0.9255 | 0 | 0.1387 | 0.9457 | 0.9721 | 0.0396 | 0.0169 |
| 3 | Img3 | 0.9651 | 0.9822 | 0.0216 | 0.0141 | 0.9210 | 0.9589 | 0.0082 | 0.0783 | 0.9292 | 0.9633 | 0.0686 | 0.0071 |
| 4 | Img4 | 0.9677 | 0.9836 | 0.0174 | 0.0155 | 0.9495 | 0.9741 | 0.0082 | 0.0427 | 0.9278 | 0.9626 | 0.0755 | 0.0021 |
| 5 | Img5 | 0.9647 | 0.9820 | 0.0044 | 0.0311 | 0.9285 | 0.9629 | 0.00008 | 0.0715 | 0.9447 | 0.9715 | 0.0492 | 0.0088 |

| | | | | | | | | | | | | | |
|---|---|---|---|---|---|---|---|---|---|---|---|---|---|
| 6 | Img6 | 0.9583 | 0.9787 | 0.0076 | 0.0344 | 0.8725 | 0.9319 | 0 | 0.1275 | 0.9426 | 0.9705 | 0.0380 | 0.0216 |
| 7 | Img7 | 0.9741 | 0.9869 | 0.0060 | 0.0200 | 0.9311 | 0.9643 | 0.0007 | 0.0682 | 0.9499 | 0.9743 | 0.0435 | 0.0088 |
| 8 | Img8 | 0.9568 | 0.9779 | 0.0159 | 0.0280 | 0.9260 | 0.9616 | 0.0032 | 0.0711 | 0.9500 | 0.9743 | 0.0383 | 0.0136 |
| 9 | Img9 | 0.9535 | 0.9762 | 0.0088 | 0.0381 | 0.8969 | 0.9456 | 0.0028 | 0.1006 | 0.9463 | 0.9724 | 0.0402 | 0.0156 |
| 10 | Img10 | 0.9405 | 0.9673 | 0.0008 | 0.0588 | 0.8605 | 0.9250 | 0 | 0.1375 | 0.9187 | 0.9576 | 0.0386 | 0.0459 |

## 6. Conclusion

In this paper, a new local Chan-Vese Expectation-Maximization (LCV-EM) model for skull stripping MRI brain images is proposed. The energy functional for the proposed model consists of a global term, local EM term and a regularization term. By incorporating the local-EM term, images having intensity inhomogeneity such as MR images can be effectively skull stripped. Incorporating the information obtained from the EM algorithm results in a better segmentation of the skull from the brain tissue as compared to other brain extraction algorithms. Further, the EM algorithm is applied only to narrowbands surrounding the zeroth level set. This results in a faster computation of the EM algorithm, hence speeding up the entire process. Experiments on MR images from the OASIS dataset and the Whole Brain Atlas have demonstrated the desired segmentation performance of the proposed model on the MR images having a large amount of intensity inhomogeneity. Further, the efficiency of the model is apparent from the values of the segmentation evaluation parameters such as Jaccard coefficient, Dice coefficient, sensitivity, specificity, false positive rate, and false negative rate.

## Acknowledgement

The author wishes to express her gratitude to Mrs. Shalini S. Mirajkar and Mr. Shashikant M. Mirajkar for their constant support and encouragement.

## References

[1] H. Zhuang, D. J. Valentino, and A. W. Toga, “Skull stripping magnetic resonance images using a model-based level set, ” NeuroImage, vol. 32, pp. 79 – 82, 2006

[2] H. Rifai, I. Bloch, S. Hutchinson, J. Wiart, and L. Garnero, “Segmentation of the skull in MRI volumes using deformable model and taking the partial volume effect into account, ” Medical Image Analysis, vol. 4, pp. 219 – 233, 2000

[3] DeCarli, J. Maisog, D. G. M. Murphy, D. Teichberg, S. I. Rapoport, and H. Horwitz, “Method for quantification of brain ventricular and subarachnoid CSF volumes from MR images, ” J. Comput. Assist. Tomogr., vol. 16, no. 2, pp. 274 – 284, 1992

[4] Lee, S. Huh, T. A. Keller, and M. Unser, “Unsupervised connectivity-based thresholding segmentation of mid-saggital brain MR images, ” Comput. Biol. Med., vol. 28, pp. 309 – 338, 1998

[5] S. Huh, T. A. Keller, K. H. Sohn, and C. S. Lee, “Automated cerebrum segmentation from 3-D saggital brain MR images, ” Comput. Biol. Med., vol. 32, pp. 311 – 328, 2002

[6] W. Shattuck, S. R. Sandor-Leahy, K. A. Schaper, D. A. Rottenburg, and R. M. Leahy, “Magnetic resonance image tissue classification using a partial volume model, ” NeuroImage, vol. 13, pp. 856 – 876, 2001

[7] G. B. Abountanos, J. Nikanne, N. Watkins, and D. M. Dawant, “Model creation and deformation for the automatic segmentation of the brain in MR images, ” IEEE Trans. Biomed. Engg., vol. 46, no. 11, pp. 1346 – 1356, 1999

[8] X. Zeng, L. H. Staib, R. T. Schulz, and J. S. Duncan, “Segmentation and measurement of the cortex from 3-D MR images using coupled-surfaces propagation, ” IEEE Trans. Med. Images, vol. 18, no. 10, pp. 927 – 937, 1999

[9] J. S. Suri, “Two-dimensional fast magnetic resonance brain segmentation, ” IEEE Trans. Med. Biol., pp. 84 – 95, 2001

[10] C. Baillard, P. Hellier, and C. Barillot, “Segmentation of brain 3D MR images using level sets and dense registration, ” Med. Image Anal., vol. 5, pp. 185 – 194, 2001

[11] S. M. Smith, “Fast robust automated brain extraction, ” Hum. Brain Mapp., vol. 17, pp. 143 – 155, 2002

[12] Y. Zhang, J. Michael Brady, and S. M. Smith, “An HMRF-EM algorithm for partial volume segmentation of brain MRI, ” FMRIB Technical Report TR01YZ1

[13] T. Géraud, L. Aurdal, H. Maitre, I. Bloch, and C. Adamsbaum, “Estimation of partial volume effect using spatial context. Application to Morphometry in cerebral imaging, ” Nuclear Science Symposium and Medical Imaging Conference Record, vol. 3, pp. 1485 – 1487, 1995

[14] “The devil’s in the detail: pixels, matrices, and slices”, in MRI From Picture to Proton, eds., D. W. McRobbie, E. A. Moore, M. J. Graves, and M.R. Prince, Cambridge University Press, 2003

[15] H. Soltanian-Zadeh and J. P. Windham, “Optimal processing of brain MRI, ” in Image Processing Techniques for Tumor Detection, eds., R. N. Strickland, 2002

[16] P. Santago and H. Gage, “Quantification of MR brain images by mixture density and partial volume modeling, ” IEEE Trans. Med. Imaging, vol. 12, no. 3, pp. 566 – 574, 1993

[17] M. Desco, J. D. Gispert, S. Reig, A. Santos, J. Pascau, N. Malpica, and P. Garcia-Barreno, “Statistical segmentation of multidimensional brain datasets, ” Proc. SPIE, Medical Imaging 2001: Image Processing, vol. 4322, pp. 184 – 193, 2001

[18] M. A. Balafar, “Spatial based Expectation Maximizing, ” Diagnostic Pathology, vol. 6, no. 103, pp. 1 – 14, 2011

[19] L. Pham and J. L. Prince, “Robust unsupervised tissue classification in MR images, ” in Proceedings of the 2004 IEEE International Symposium on Biomedical Imaging: Macro to Nano, pp. 109 – 112, 2004

[20] K. V. Leemput, F. Maes, D. Vandermeulen, and P. Seutens, “A unifying framework for partial volume segmentation of brain MR images, ” IEEE Trans. Med. Imag., vol. 22, no. 1, pp. 105 – 119, 2003

[21] K. Held, E. R. Kops, B. J. Krause, W. M. Wells, R. Kikinis, and H. Muller-Gartner, “Markov-random field segmentation of brain MR images, ” IEEE

Trans. Med. Imag., vol. 16, no. 6, pp. 878 – 886, 1996

[22] K. V. Leemput, F. Maes, D. Vandermulen, and P. Seutens, “Automated model-based tissue classification of MR images of the brain, ” IEEE Trans. Med. Imag., vol. 18, no. 10, pp. 897 – 908, 1999

[23] W. M. Wells, W. E. L. Grimson, R. Kikinis, and F. A. Jolesz, “Adaptive segmentation of MRI data, ” IEEE Trans. Med. Imag., vol. 15, pp. 429 – 442, 1996

[24] D. Mumford and J. Shah, “Optimal approximation by piecewise smooth function and associated variational problems, ” Commun. Pure Appl. Math. Vol. 42, pp. 577 – 685, 1989

[25] T. F. Chan and L. A. Vese, “Active contours without edges, ” IEEE Trans. Image Process., vol. 10, no. 2, pp. 266 – 277, 2001

[26] S. Osher and J. A. Sethian, “Fronts propagating with curvature-dependent speed: algorithms based on Hamilton-Jacobi formulations, ” J. Comput. Phys., vol. 79, no. 1, pp. 12 – 49, 1988

[27] D. E. Maroulis, M. A. Savelonas, D. K. Iokovidis, S. A. Karkanis, and N. Dimitropoulos, “Variable background active contour model for computer-aided delineation of nodules in thyroid ultrasound images, ” IEEE Trans. Inf. Technol. Biomed., vol. 11, no. 5, pp. 537 – 543, 2007

[28] Cohen and L. D. Cohen, “A hybrid hyperquadratic model for 2-D and 3-D data fitting, ” in 12th IEEE International Conference on Pattern Recognition (ICPR’94), vol. B, pp. 403 – 405, 1994

[29] S. Lobregt and M. A. Viergever, “A discrete dynamic contour model, ” IEEE Trans. Med. Imag., vol. 14, no. 1, pp. 12 – 24, 1995

[30] V. Caselles, F. Catte, T. Coil, and F. Dibos, “A geometric model for active contours in image processing, ” Numer. Math., vol. 66, no. 1, pp. 1 – 3, 1993

[31] V. Caselles, R. Kimmel, and G. Sapiro, “Geodesic active contours, ” Int. J. Comput. Vision, vol. 22, no. 1, pp. 61 – 79, 1997

[32] R. Malladi, J. A. Sethian, and B. C. Vermuri, “Shape modeling with front propagation: a level set approach, ” IEEE Trans. Pattern Anal. Mach. Intell., vol. 17, no. 2, pp. 158 – 175, 1995

[33] Tsai, A. Yezzi, and A. S. Willsky, “Curve evolution implementation of the Mumford-Shah functional for image segmentation, denoising, interpolation, and magnification, ” IEEE Trans. Image Process., vol. 10, no. 8, pp. 1169 – 1186, 2001

[34] P. Dempster, N. M. Laird, and D. B. Rubin, “Maximum likelihood from incomplete data via the EM algorithm, ” J. R. Stat. Soc., vol. 39, pp. 1 – 38, 1977

[35] W. M. Wells, III, W. E. L. Grimson, R. Kikinis, and F. A. Jolesz, “Adaptive segmentation of MRI data, ” IEEE Trans. Med. Imag., vol. 15, pp. 429 – 442, 1996

[36] Z. Liang, J. R. MacFall, and D. P. Harrington, “Parameter estimation and tissue segmentation from multispectral MR images, ” IEEE Trans. Med. Imag., vol. 13, pp. 441 – 449, 1994

[37] F. J. Wu, “On the convergence properties of the EM algorithm, ” Ann. Stat., vol.

11, no. 1, pp. 95 – 103, 1983

[38] Y. H. Tsai and S. Osher, "Total variation and level set based methods in image science, " Acta Numer., pp. 1 – 61, 2005

[39] M. Sussman and E. Fatemi, "An efficient interface preserving level set redistancing algorithm and its application to interfacial incompressible fluid flow, " SIAM J. Sci. Comput., vol. 20, pp. 1165 – 1191, 1999

[40] Mirajkar, "An accuracy based comparison of three brain extraction algorithms, " International Journal of Computer Applications, vol. 49, no. 18, pp. 45 – 51, 2012

[41] P. Jaccard, "The distribution of flora in Alpine zone, " New Phytol., vol. 11, no. 2, pp. 37 – 50, 1912

[42] P. Zijdenbos, B. M. Dawant, R. A. Margolin, and A. C. Palmers, "Morphometric analysis of white matter lesions in MR images, " IEEE Trans. Med. Imag., vol. 13, pp. 716 – 724, 1994

[43] K. V. Leemput, F. Maes, D. Vandermeulen, and P. Suetens, "Automated model-based bias field correction of MR images of the brain, " IEEE Trans. Med. Imag., vol. 18, no. 10, 1999

[44] X-F Wang, D-S Huang, and H. Xu, "An efficient local Chan-Vese model for image segmentation, " Pattern Recog., vol. 43, pp. 603 – 618, 2010

## Summary

Intracranial brain segmentation commonly referred to as skull-stripping, aims to segment the brain tissue (cortex and cerebellum) from the skull and non-brain intracranial tissues in magnetic resonance (MR) images of the human brain. Skull stripping forms an important pre-processing step in neuroimaging analyses. In this paper, a local Chan-Vese Expectation Maximization (LCV-EM) model is proposed for skull segmentation which uses both global image information and the local information obtained via the EM algorithm. The energy functional for the proposed model consists of three terms: the global term, local EM term, and the regularization term. Since MR images contain a lot of intensity inhomogeneity, the use of the local-EM term along with the global information allows the skull and non-brain tissue to be segmented from the brain tissue in spite of the partial volume effect prominent near the boundary of the skull. The LCV-EM model is applicable to both T1 and T2-weighted MR images. The model has the advantage that it does not require any boundary function or stopping function to decide the true boundary of the skull. Also, the problem of leakage through the boundary can be eliminated through the choice of the width of the interior and exterior narrowbands surrounding the evolving contour. The model also shows good performance in comparison with other methods for brain extraction such as BSE, skull stripping using GAC, and the Chan-Vese model and also provides good segmentation results even in the presence of noise. Experiments on MR images from the OASIS dataset and the Whole Brain Atlas have demonstrated the desired segmentation performance of the model. The efficiency of the model is also apparent from the values of segmentation evaluation parameters such as Dice coefficient, false positive rate and false negative rate.